Aerosp. Sci. Technol. 142 (2023) 108638

Contents lists available at ScienceDirect

Aerospace Science and Technology

journal homepage: www.elsevier.com/locate/aescte

A geometric sensitivity study for the aerodynamics of a strut-braced airframe

B. Jones *, P. Nagy, E. Minisci, M. Fossati

Aerospace Centre, Department of Mechanical and Aerospace Engineering, University of Strathclyde, 75 Montrose street, G1 1XJ, Glasgow, United Kingdom

ARTICLE INFO

Communicated by Mehdi Ghoreyshi

Keywords:
Aerodynamics
Strut-braced wings
Reduced order modelling
Sensitivity analysis

ABSTRACT

A global sensitivity analysis method, the adaptive-cut high-dimensional model representation method (HDMR) is considered to evaluate the impact of geometrical changes of a ultra-high aspect ratio strut-braced wing configuration on the aerodynamic performance. A data-driven reduced order model based on Proper Orthogonal Decomposition is used to keep the computational cost of the analysis at a manageable level. The airframe configuration is described using 7 geometrical parameters, which comprise the design space. The geometrical parameters are decomposed and analysed across their whole range of values by the HDMR to assess their influence on the Drag coefficient, Lift coefficient and Lift-to-Drag ratio of the aircraft. These results form the basis for a qualitative exploration of the aerodynamics of such airframes further augmented by high-fidelity CFD simulations. Results show that the sweep angle of the wing is the dominant parameter in terms of Drag due to changes in shock wave intensity. Changes in the wing root chord also implicitly affect the local geometry at the wing-strut junction, which influences the blockage effect and thus the intensity of the shock waves at the junction. Lift is affected primarily by the twist of the wing. Overall, the strut is shown to have significant effects on the performance of the aircraft design due to the presence of strong shock waves at the wing-strut junction and interference effects.

1. Introduction

The climate crisis necessitates increasingly aggressive emissions goals for the aviation industry. Authorities in Europe and the United States are continuously developing and refining decarbonisation agenda aiming to achieve net-zero greenhouse gas emissions in the aviation sector by 2050 [1,2]. It is now widely recognised that the required reduction of emissions can be effectively achieved by the exploration and TRL advancement of unconventional aircraft technologies [3]. With numerous efforts targeting step improvements in aerodynamics, structures and propulsion, enabling the use of ultra-high aspect ratio (UHAR) wings is seen as one key priority to reduce fuel consumption by improving aerodynamic performance, possibly reducing structural weight and facilitating advanced distributed propulsion concepts.

A popular UHAR airframe configuration that has been subject to numerous studies employs wings with large span supported by a strut, the so-called strut-braced wing (SBW) configuration [4–7]. Despite the recent efforts dedicated to the study of the aerodynamic behaviour of SBW airframes, still more insight is needed to consolidate the understanding of such airframes when it comes to interpreting the impact that changes in the geometry have on the aerodynamic performance, such as Lift, Drag and Lift-to-Drag ratio. The complex aerodynamic environment in critical areas such as the strut-wing intersection is deemed to significantly depend on parameters such as wing and strut sweep, span, twist, airfoils, and a dedicated sensitivity study is required to make informed design decisions.

Global sensitivity analysis allows the effect on parameter(s) of interest to be linked with changes in the design parameters, as opposed to local sensitivity analysis which focuses on the derivatives of a function around a single design point [8].

Gong and Ma performed a variance-based global sensitivity analysis on surrogates of high-fidelity computational fluid dynamics (CFD) analyses of morphing-wing aircraft [9]. They showed that in the transonic regime, when considering the span, root chord, and sweep, the span of the wing accounts for 84% of the variance in the Lift-to-Drag ratio (L/D). Chakraborti et al. performed a global sensitivity study on optimised truss-braced wing conceptual designs with varying span and a varying number of juries, to investigate whether increases in span – which pose various design issues such as geometric nonlinearity and

* Corresponding author.
E-mail address: bryn.jones@strath.ac.uk (B. Jones).

https://doi.org/10.1016/j.ast.2023.108638
Received 13 June 2023; Received in revised form 12 September 2023; Accepted 12 September 2023
Available online 22 September 2023

Table 1
Bounds of design space of the SBW configuration test case.

Parameter	Minimum	Maximum	Strut length [m]	Strut sweep [deg]
Wing sweep [°]	5.0	15.0	13.13 | 13.15	4.3 | 14.4
Wing span [m]	28.7	33.0	12.06 | 14.21	9.4 | 9.4
Root chord [m]	2.7	3.3	13.14 | 13.14	9.2 | 9.6
Tip chord [m]	0.9	1.3	13.14 | 13.14	9.4 | 9.4
Kink twist [°]	-1.0	0.0	13.14 | 13.14	9.4 | 9.4
Tip twist [°]	-2.0	-0.8	13.14 | 13.14	9.4 | 9.4
Strut incidence [°]	-3.0	0.0	13.14 | 13.14	9.4 | 9.4
Aspect ratio	20.4	29.3	-	-

airport serviceability – are necessary to achieve desired objectives [10]. By constraining their conceptual multidisciplinary optimisation to different maximum spans, they found that despite a clear improvement in L/D as the span constraint is relaxed, the improvement in fuel burn diminishes as the span increases past 170 feet (aspect ratio 16.6), possibly due to increases in structural weight. Another SBW conceptual design study by Hosseini et al. showed that increases in aspect ratio in the range of 15 to 23 lead to nearly linear improvements in cruise L/D from 21 to 24 [11].

An optimisation study performed by Chau and Zingg on a SBW aircraft showed that the optimal strut Lift is negative towards the attachment point to reduce pressure gradients, with the wing design compensating for this by producing more Lift locally to bring the total Lift distribution closer to an elliptic curve [12]. In turn, this Lift compensation causes the optimal wing twist to follow a relatively flat distribution between 0.2 wing spans and the strut attachment point when compared with an optimal conventional tube-and-wing configuration, before dropping off further outboard towards the tip to produce the necessary washout. An SBW optimisation performed by Secco and Martins showed that the optimiser prefers a negative Lift on the strut, achieved in part by a negative strut twist, to eliminate shock and separation at the intersection [13].

Although these studies provide valuable insights, there is a gap in the knowledge in terms of a comprehensive global high-fidelity sensitivity analysis with many geometrical parameters. In this work, a global sensitivity analysis based on adaptive-cut high-dimensional model representation (HDMR) [14,15] and data-driven Reduced Order Modelling (dd-ROM) [16] is presented to explore the effect of changes in several high-level geometrical parameters on the Lift and Drag for a SBW airframe which resulted from a conceptual design process [17].

The HDMR analysis allows the identification of the most important parameters, i.e. the sensitivity rankings, and allows the exploration of the parameter interactions. In addition to a qualitative analysis, the same HDMR approach allows quantitative evaluations of the changes in aerodynamic loads and the quantification of the gradients of aerodynamic coefficients with respect to the geometry. The use of dd-ROM [16,18] is here proposed as a way to keep a moderate computational cost for the HDMR iterative process while ensuring that the accuracy of the evaluations of the aerodynamic performance is comparable to high-fidelity CFD.

The manuscript is organised as follows: Section 2 presents the geometry definitions and parameterisation of the UHAR-SBW airframe together with the high-fidelity and dd-ROM methods used to evaluate the aerodynamic performance. Section 3 introduces the HDMR methodology and its validation for the SBW airframe under consideration. Sections 4 and 5 present the results of the analysis respectively for C_L and C_D. Section 6 presents the results for L/D based on the ratio of surrogates for C_L and C_D. Finally Section 7 discusses the results of the dd-ROM based sensitivity by means of high-fidelity CFD verification.

Table 2
Definitions of the nominal (central) configuration for the sensitivity study.

Wing sweep [°]	10	Tip twist [°]	-1.4
Wing span [m]	30.85	Strut incidence [°]	-1.5
Root chord [m]	3	Aspect ratio	24.4
Tip chord [m]	1.1	Strut length [m]	13.14
Kink twist [°]	-0.5	Strut sweep [m]	9.4

2. Geometric and aerodynamic modelling

2.1. Geometric parameterisation of a strut-braced wing airframe

The SBW aircraft configuration studied in this work was defined as part of a recent conceptual design study [17]. The study made use of a modified version of SUAVE [19] to analyse and compare conceptual strut-braced wing and twin-fuselage aircraft configurations at three mission ranges. The results showed that the twin-fuselage configuration performs better in mid-range and long-range scenarios, however the strut-braced wing was selected due to having a higher technology readiness level.

Seven planform parameters were then considered for a preliminary design MDO study: wing sweep, wing span, chord at wing root, chord at wing tip, twist angle at kink section, twist angle at the wing tip and incidence angle of the strut. A DOE of high-fidelity RANS CFD solutions was produced for the RHEA project for the purposes of the MDO study, which is then re-used for the purposes of global sensitivity analysis in this paper. Other parameters such as those describing the wing/strut intersection may also be important for SBW aircraft, however, the parameter list is necessarily kept small to minimise the dimensionality of the problem, resulting in these parameters being prioritised over others.

The airfoils at root, kink and wingtip are supercritical airfoils. Ideally, these could be re-optimised for each change in the geometrical parameters, however the whole analysis has been conceived to be relevant at the level of a conceptual design phase, where the computational demand required by the further optimisation of the airfoil shape may not always be justified or feasible. The airfoil of the strut is a symmetric NACA 64A-018, and its intersection is fixed at 50% wing span, where the value was chosen as a compromise of aerodynamic and structural considerations. Table 1 shows the range for each of the seven geometric parameters that are considered in the present study, while Table 2 shows the values of the parameters for the nominal (central) aircraft configuration. The last row of Table 1 reports the minimum and maximum aspect ratio values within the parameter space.

It is worth noting that, as a consequence of the choice of Table 1, changes in some of the parameters lead to changes in the geometry of the strut, i.e. its sweep angle, its span and the local geometry near the wing-strut junction. Since this can significantly influence the aerodynamic behaviour, the extent to which each parameter affects the strut geometry is reported in the last two columns of Table 1.

The left side of Fig. 1 shows the nominal configuration considered for this study, while the right side shows a representation of the central configuration by means of a normalised spider plot. Fig. 2 shows an overlay of two geometries corresponding to opposite corners of the pa-

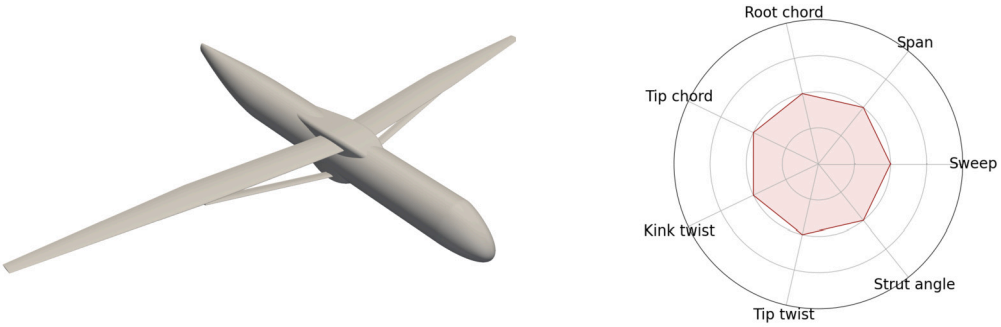

Fig. 1. Nominal configuration of the SBW aircraft (left), abstract representation via spider plot (right).

Fig. 2. Overlay of the SBW configuration at the minimum (white) and maximum (black) bounds of the geometrical parameter space.

Table 3
Freestream conditions of the test case.

Mach number	Reynolds number	Angle of Attack	Temperature
0.735	16,665,920	2.5°	222.78

rameter space; one with all the parameters set to the minimum value, and the other with all parameters set to the maximum value. The pronounced effect on the strut is also shown.

2.2. Evaluation of aerodynamic performance: CFD and data-driven Reduced Order Modelling

The HDMR adaptive sampling process requires evaluations of the aerodynamic coefficients at arbitrary locations in the geometric parameter space. CFD simulations provide an excellent evaluation of the aerodynamics, but have an excessive computational cost when many evaluations are required, as is the case in this global sensitivity analysis study with a 7-dimensional parameter space.

Therefore, a data-driven Reduced Order Modelling approach based on Proper Orthogonal Decomposition (POD) [20] is introduced. The proposed approach aims at computing a set of CFD solutions over the parameter space and use this set to train the POD-based ROM. The generation of this training set is performed offline prior to the HDMR process, only once, and in a highly parallelised manner. Then the online requirement of aerodynamic evaluation is fulfilled by invoking the POD-based ROM, resulting in substantial savings of both computational and wall clock time.

The training set of CFD solutions are obtained using the open-source CFD code SU2 [21], based on the Finite Volume method. Steady-state RANS solutions are computed using the Roe upwind scheme with MUSCL approach to obtain a second-order approximation, and turbulence is solved using the Spalart-Allmaras model. The constant freestream conditions are listed in Table 3. Solutions are collated into a snapshot set which forms the basis of the aerodynamic ROM.

The parameter space is sampled so that a CFD solution is computed at each corner, corresponding to 128 geometries, with an additional 67 geometries from inside the bounds of the space based on the Sobol sequence. The snapshot set is thus constructed from 195 solutions. While the CFD simulations are computed on the aircraft half-body, the aerodynamic ROM is created only for the wing and strut, thus the sensitivity analysis is performed considering only those two components.

The POD-based ROM considered in this work is a widely known non-intrusive model order reduction approach that seeks a linear space approximating the solution manifold by extracting the optimal basis functions from the training set of CFD solutions. The optimal property of POD refers to the fact that the error between the training data and its truncated representation is minimised, specifically under the L^2 norm. Thus, the POD modes are identified by solving the maximisation problem [20]:

$$\max_{\psi} \frac{\langle |(\mathbf{U}, \boldsymbol{\psi})^2| \rangle}{(\boldsymbol{\psi}, \boldsymbol{\psi})} = \frac{\langle |(\mathbf{U}, \boldsymbol{\phi})^2| \rangle}{(\boldsymbol{\phi}, \boldsymbol{\phi})} \tag{1}$$

where $\mathbf{U}$ is the snapshot set: $\{\mathbf{u}_1, \mathbf{u}_2, \ldots, \mathbf{u}_{N_s}\}$ for N_s CFD solutions, and $\boldsymbol{\phi}$ are the sought basis functions from the maximisation process under the prospective basis functions ψ. The operators $(\cdot, \cdot)$ and $\langle \cdot \rangle$ denote the inner product and averaging across the parameter space respectively.

The algorithm adopted in this work is the *method of snapshots* approach proposed by Sirovich [22]. Following this approach it is shown that the basis functions can be expressed as a linear combination of the snapshot set:

$$\boldsymbol{\phi}_i = \sum_{j=1}^{N_s} b_j^i \mathbf{u_j} \tag{2}$$

for $i = 1, 2, \ldots, N_s$. $\mathbf{u_j}$ is the quantity of interest for snapshot j, and b_j^i is the associated POD coefficient. The coefficients b_j^i satisfy the eigenvalue problem:

$$\mathbf{R}\mathbf{b}_i = \lambda_i \mathbf{b}_i \tag{3}$$

where $\mathbf{R} = \mathbf{U}^T\mathbf{U}$, i.e. the cross-correlation matrix of the snapshots. The energy associated with each mode is given by the eigenvalues λ_i, in essence quantifying the relative importance of a mode [18].

Thus, the modes can be ordered according to their energy content and truncated based on a threshold energy content. Since the number of DoF in the low-dimensional model is given by the number of POD modes, an efficient order reduction is achieved in this way [16]. The normalised POD modes are expressed as:

$$\phi_i = \frac{1}{\sqrt{\lambda_i}} \mathbf{U}\mathbf{b}_i \tag{4}$$

Table 4
Time statistics for the CFD and the generation of the dd-ROM.

CFD volume mesh	17M nodes
Surface mesh (wing and strut only)	265,937 nodes
Core-hours for single snapshot (DATA - off-line)	1,008
Core-hours to build ROM (LEARNING - off-line)	0.1 (6 min)
Core-hours for single ROM (PREDICTION - on-line)	0.017 (1 min)
Core-hours for full dd-ROM HDMR study	24

The solution at any location in the parameter space is eventually expressed as a linear combination of the POD modes and their associated coefficients, a_i. The coefficients are obtained by way of Radial Basis Function (RBF) interpolation. Then a reconstructed solution is computed as:

$$\mathbf{u}(\mathbf{x}) \approx \hat{\mathbf{u}} = \sum_{i=1}^{N_m} a_i \phi_i(\mathbf{x}) \tag{5}$$

One of the advantages of this method in contrast to classical POD is that instead of operating on the snapshot set directly, the eigenvalue decomposition of the cross-correlation matrix is calculated, which reduces the computational complexity of the low order model significantly. A similar, interpolation-based non-intrusive approach is presented by Bui-Tanh et al. [18].

The POD approach is trained based on the pressure and skin friction field quantities of the whole wing and strut surfaces, rather than on the scalars of interest C_L and C_D. This results in a larger ROM computational cost, but more information is conserved, surface solutions may be reconstructed, and the calculation of C_L and C_D is more physical, coming from the integration of surface fields rather than direct interpolation. Table 4 reports the size of the computational mesh and the time statistics for the generation of the training set as well as the on-line execution time of the dd-ROM.

2.3. Validation of the POD approach

A leave-one-out error analysis is performed on the ROMs, where each snapshot is iteratively excluded from the training set so that it can be used as a point to estimate the error of the dd-ROM based on $N_S - 1$ snapshots. The error of the dd-ROM is therefore characterised by assessing the accuracy of slightly different dd-ROMs over the parameter space.

Given the nature of the leave-one-out approach, the error estimate can be considered to be a conservative measure since the actual dd-ROM used in the HDMR analysis uses all the existing snapshots and therefore will represent more physics than any one of the N_S different dd-ROMs generated on the basis of $N_S - 1$ snapshots.

Fig. 3 reports the errors on pressure over the wing and the strut on the left and the error on L/D ratio on the right side. The error on pressure is computed as follows,

$$\begin{aligned} E_{\mathrm{P,wing}} &= \mathrm{rms}|P_{i,\mathrm{POD}} - P_{i,\mathrm{CFD}}| \quad \text{for} \quad i = 1, \ldots, N_{\mathrm{g,wing}} \\ E_{\mathrm{P,strut}} &= \mathrm{rms}|P_{j,\mathrm{POD}} - P_{j,\mathrm{CFD}}| \quad \text{for} \quad j = 1, \ldots, N_{\mathrm{g,strut}} \end{aligned} \tag{6}$$

where $N_{\mathrm{g,wing}}$ and $N_{\mathrm{g,strut}}$ indicate respectively the number of grid points on the surface of the wing and the strut. Separate errors are computed and shown for the wing and the strut, see Fig. 3 left.

The estimation of the error on Lift-to-Drag ratio is obtained by computing first the pressure and the shear stress on the surface of the wing and the strut via the dd-ROM, integrating the local loads over the surface and then comparing with the available CFD values,

$$E_{\mathrm{L/D}} = (L/D)_{\mathrm{POD}} - (L/D)_{\mathrm{CFD}} \tag{7}$$

The highest error in Lift-to-Drag ratio is approximately 11.5% of the corresponding CFD value. Due to the difficulty in representing 7-dimensional data set, the errors are presented in Fig. 3 by ordering the snapshots by their ID, i.e. the horizontal axis in the plots.

Table 5
Error in the aerodynamic coefficients for the leave-one-out POD reconstruction with the maximum root mean square pressure error on the strut.

	CFD	POD	Error
$\mathbf{C_L}$	0.352	0.344	2.3%
$\mathbf{C_D}$	162 d.c.	160 d.c.	2 d.c.

Figs. 4 and 5 show the spider plots corresponding to the configurations exhibiting the highest error in pressure over the wing and over the strut, respectively. Specifically, the latter is the configuration with the sweep, tip twist, and strut angle at the maximum values, and everything else at the minimum. For this specific geometry, Table 5 shows the corresponding error in the function of interest, namely the aerodynamic coefficients. It is observed that this error is small even for this point exhibiting the largest root mean square error in pressure.

A visual assessment of the error is provided via a direct comparison of the pressure and skin friction fields on the wing and strut as shown in Figs. 6 and 7. The configuration being shown here is the one corresponding for the one in Fig. 5. The main features of the flow are captured well, however key differences arise in the area surrounding the shock near the strut-wing junction. This discrepancy is more pronounced for shear stress where slight errors in the location of the shock wave may induce significant local errors in skin friction and pressure loads.

3. Adaptive-cut high-dimensional model representation

The Adaptive-cut High Dimensional Model Representation (A-cut-HDMR) [23,14,15] is a probabilistic non-intrusive method similar to the Analysis Of Variance, ANOVA, decomposition. The A-cut-HDMR approach decomposes the general function response, $f(\mathbf{U})$ to a sum of the contributions given by each variable and each one of their interactions through the model, considered as increments with respect to the response in the anchor point (not necessarily the nominal response), f_c:

$$f(\mathbf{U}) = f_c + \sum_{i=1}^{N_u} F_i(U_i) + \sum_{i<j<=N_u} F_{i,j}(U_i, U_j) + \ldots + F_{1,2,\ldots,N_u}(U_1, U_2, \ldots, U_{N_u}), \tag{8}$$

where N_u is the number of parameters, F_i, $i = 1, \ldots, N_u$, are the orthogonal incremental contributions of every single parameter, $F_{i,j}, 1 <= i < j <= N_u$, are the incremental contributions of each pair of parameters and $F_{1,2,\ldots,N_u}$ is the incremental contribution of the interaction of all the parameters.

A surrogate model representation is independently generated for each incremental contribution and only for the non-zero elements, thus greatly reducing the complexity of sampling and building the model. Moreover, the contribution of each term of the sum to the global response is quantified independently so that higher-order interactions with low or zero contribution are neglected already by analysing the lower-order terms. The only assumption is the independence of the inputs.

Not only is the output of this method the distribution of the quantity of interest, but also the quantification of the global contribution of each term of the sum to the global response. This feature gives a key advantage of the method by allowing for a complete analysis of the sensitivity of the response with respect to each of the variables, as well as their interactions, greatly limiting the computational cost for high-dimensional problems.

Moreover, in the case that the output function of interest is given by a black-box model, the analysis of the single contributions provides insight into the structure of the response function. The surrogate mod-

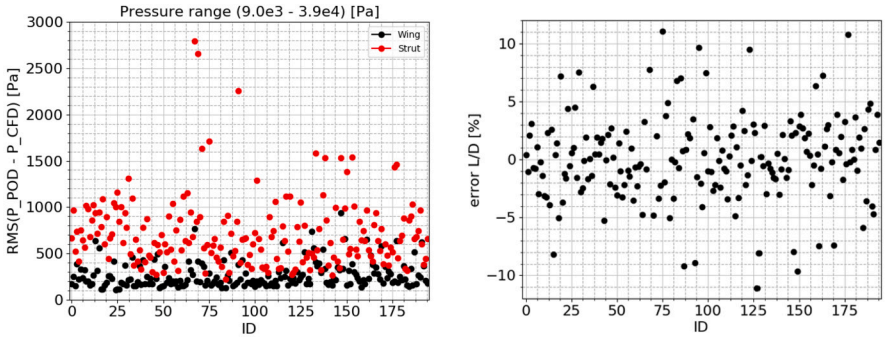

Fig. 3. Plot of root mean square error of each surface pressure field from the leave-one-out analysis and the error in Lift-to-Drag ratio.

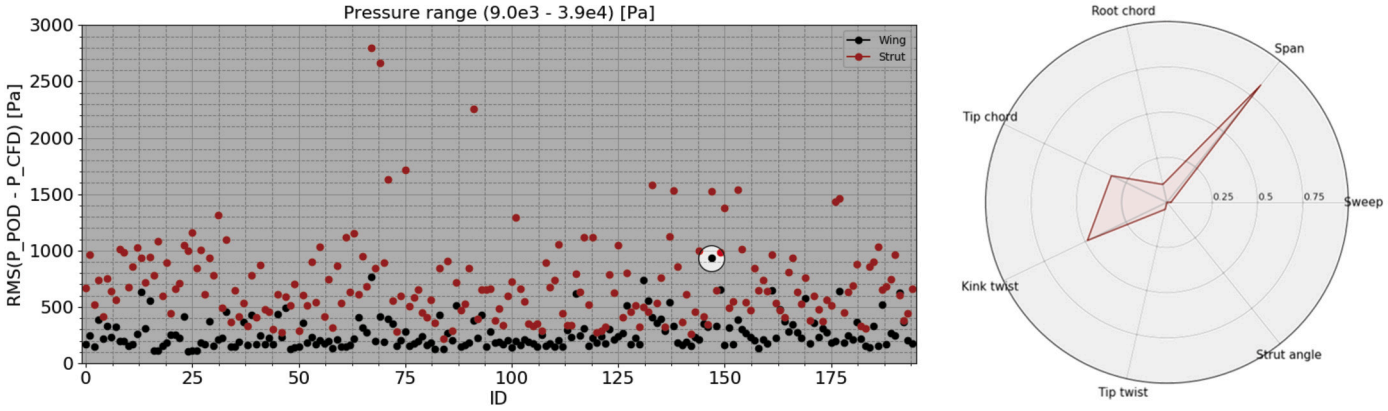

Fig. 4. Spider plot corresponding to the point with the highest rms error on the wing.

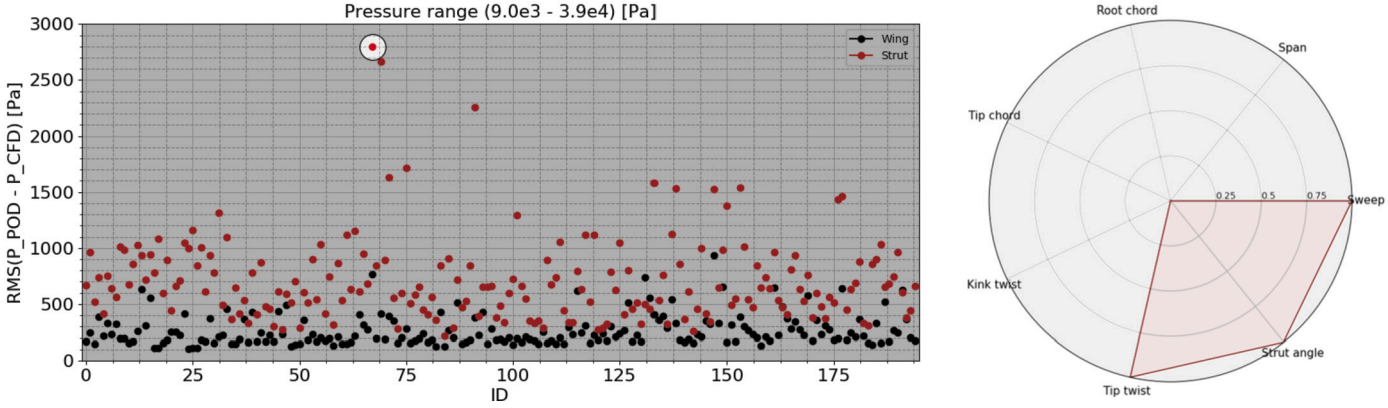

Fig. 5. Spider plot corresponding to the point with the highest rms error on the strut.

elling also allows for various post-processing visualisations based on the input parameters in a computationally efficient manner.

The A-cut-HDMR is adaptive in terms of sampling and truncation of terms in Eq. (8). The adaptive sampling takes into account the shape of the underlying response and also the input distributions, leading to an efficient distribution of samples for the considered parameters and combinations. The adaptive truncation removes the interactions that give a contribution to the overall response lower than a predefined threshold. The implemented heuristics for additivity have been demonstrated to be robust and efficient on a broad range of engineering cases.

3.1. Problem definition

Since the HDMR is non-intrusive, it needs only a "black box" interfacing function whose inputs are the design parameters and whose output is the parameter of interest, and a set of distributions corresponding to the inputs which define the exploration of the sensitivity study.

In this case, the inputs are the seven geometrical parameters of the aerodynamic ROM, with uniform distributions whose bounds match the bounds of the initial DoE. The uniform distributions ensure both that bias is not introduced in any particular area of the DOE space, and that samples are not taken outside of the DOE, which would lead to extrapolation. The sensitivity analysis is performed for each of the two output parameters, namely the Drag coefficient C_D and the Lift coefficient C_L.

In the online process, the HDMR method builds low-order subdomain surrogates, which interpolate directly values of C_L or C_D as a function of one or more geometrical parameters. These surrogates are based upon integrated samples of the POD surface ROM, which is described in the previous section. The surrogates are then used to further sample the POD ROM in an adaptive manner, and to provide the post-processing data.

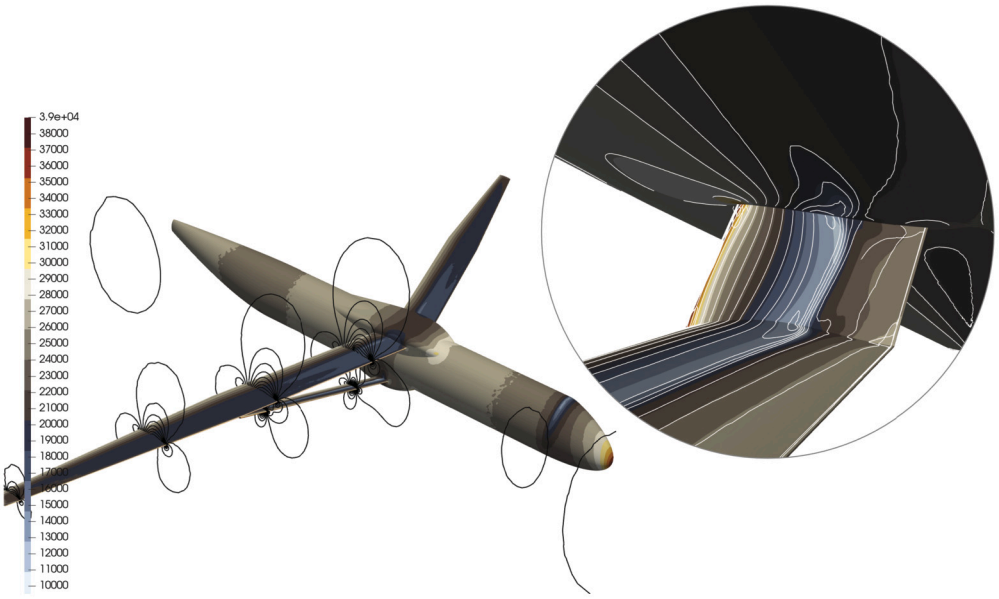

Fig. 6. Pressure [Pa] over the airframe with the highest rms error on the strut. Coloured contours are CFD, white lines are dd-ROM. Black lines show Cp at various wingspan locations. (For interpretation of the colours in the figure(s), the reader is referred to the web version of this article.)

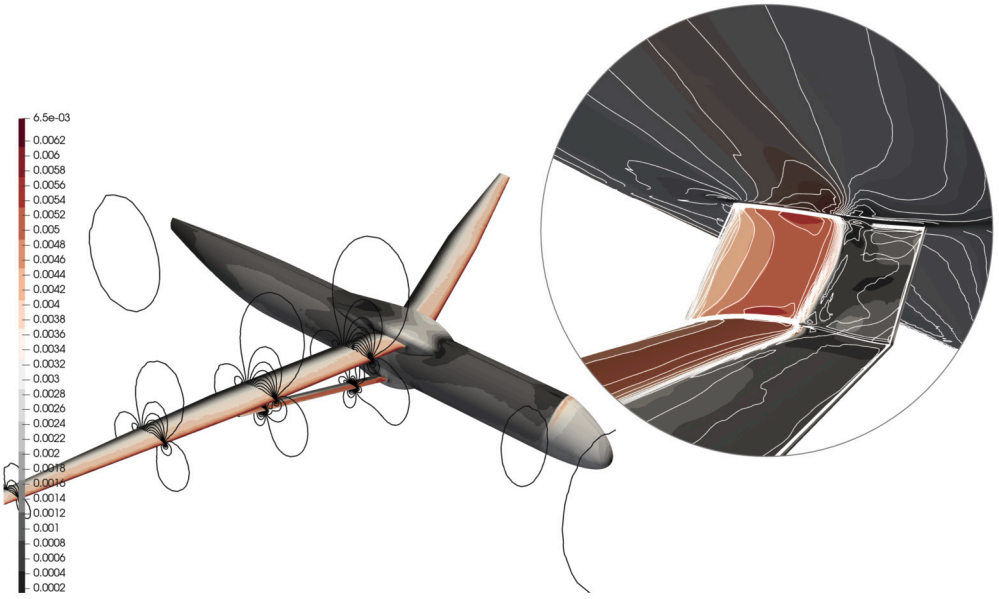

Fig. 7. Skin friction Coefficient over the airframe with the highest rms error on the strut. Coloured contours are CFD, white lines are dd-ROM. Black lines show C_P at various wingspan locations.

3.2. Validation of the adaptive-cut HDMR approach

The following subsections detail the validation of the HDMR surrogate models, starting with a validation against high-fidelity CFD solutions, followed by a validation of the HDMR surrogates against POD.

3.2.1. Error relative to CFD

Since the HDMR produces a surrogate of some integrated responses of POD reconstructions, the sensitivity analysis may be affected by two compounding levels of approximation. For this reason, both the ROM and the HDMR models are verified by comparing them against some additional CFD solutions. To this end, four samples are chosen by using a Latin hypercube approach, whose values are found in Appendix C.

The error for each of the samples is calculated via Equation (9):

$$E = \frac{C_{\text{Sur}} - C_{\text{CFD}}}{C_{\text{CFD}}}, \tag{9}$$

where E is the relative error; C_{Sur} is the surrogate aerodynamic coefficient; and C_{CFD} is the CFD aerodynamic coefficient.

The relative error for both C_L and C_D is shown in Fig. 8. In all the four cases, the POD response has an error $< 7\%$ in module, and the HDMR predicted response is $< 2\%$ different from POD.

3.2.2. Error relative to POD

Since POD is much less computationally expensive than the high-fidelity CFD analysis, many more points are selected to verify the HDMR surrogate against it. 1000 Latin hypercube samples are selected for the verification, with the error calculated via Equation (10):

$$E = \frac{C_{\text{HDMR}} - C_{\text{POD}}}{C_{\text{POD}}}, \tag{10}$$

As is shown in Fig. 9, there is some correlation between the error in the HDMR surrogate and the distance from the centre of the param-

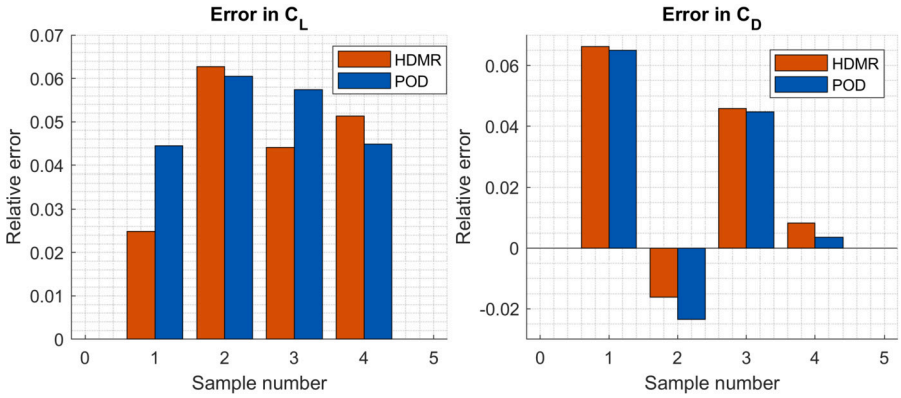

Fig. 8. Plot of the error in the aerodynamic coefficients for the POD and HDMR surrogate models relative to the results from high-fidelity CFD simulations. The value of the geometrical parameters for each of these samples is found in Appendix C.

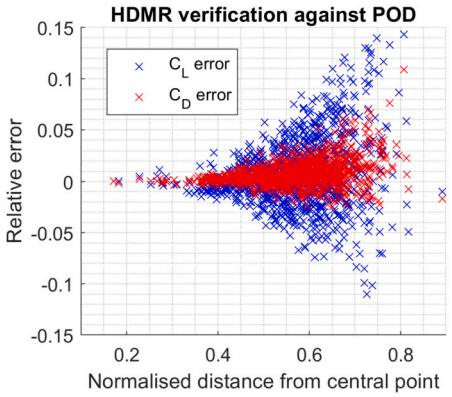

Fig. 9. Plot of the error in the coefficient of Lift and the coefficient of Drag HDMR surrogates when compared with the corresponding values from POD, against the normalised distance from the centre of the parameter space.

eter space, which is the anchor point of the HDMR. Such a correlation in the HDMR suggests that some high-order interactions should be considered, while they are neglected by the adaptive construction of the HDMR model. Relatively large errors (up to 15%) are obtained for points located near the corners of higher order neglected subdomains.

This hypothesis is tested first by constructing an analogue to the HDMR subdomain surrogates from POD solutions. For a given point in the design space $\mathbf{x}_q$, the POD analogue is constructed by mimicking the HDMR process outlined in Eq. (8).

Initially, the central value f_c is computed by replacing each of the design parameters with its corresponding central value, giving $\mathbf{x}_c$. The POD equivalent of the functional response from a first-order HDMR surrogate $F_i(U_i)$ at $\mathbf{x}_q$ is then computed by: replacing the i^{th} component of $\mathbf{x}_c$ with the i^{th} component of $\mathbf{x}_q$; evaluating POD at this point; and subtracting from this result f_c, giving r_i. Similarly, analogues of second-order surrogates $F_{i,j}(U_i, U_j)$ are evaluated by replacing both the i^{th} and j^{th} components of $\mathbf{x}_c$ with their corresponding values from $\mathbf{x}_q$, evaluating POD at this point, and subtracting from this result f_c, r_i, and r_j, giving $r_{i,j}$. Higher-order analogues are constructed following the same logic.

The POD analogue represents the value a given HDMR subdomain surrogate would take if it had zero approximation error in the context of its subdomain. Therefore, a decomposition of the total HDMR error into two components is possible. The first, which we call the "surrogate" error, is the cumulative error from each considered HDMR sub-domain surrogate relative to the POD analogue, shown in Eq. (11):

$$E_{\text{surrogate}} = \sum_{m=1}^{n} \frac{\Delta C_{\text{HDMR,m}} - \Delta C_{\text{POD,m}}}{C_{\text{POD}}}, \tag{11}$$

where $\Delta C_{\text{HDMR,m}}$ is the value of the m^{th} HDMR surrogate, e.g. $F_i(U_i)$, $F_{i,j}(U_i, U_j)$, etc. from equation (8), at a point $\mathbf{x}_q$ where we wish to evaluate the error; n is the total number of subdomains used (not truncated) by the HDMR model; $\Delta C_{POD,m}$ is the POD analogue of $\Delta C_{\text{HDMR,m}}$ as described in the previous paragraph; and C_{POD} is the actual POD value at the point $\mathbf{x}_q$.

The second, which we call the "interaction" error, is the error that occurs from neglecting high-order interactions, and is calculated as the relative error between the sum of the POD analogue of each non-truncated HDMR subdomain and the actual POD value, shown in Eq. (12):

$$E_{\text{interaction}} = \frac{(\sum_{m=1}^{n} \Delta C_{\text{POD,m}}) - C_{\text{POD}}}{C_{\text{POD}}}, \tag{12}$$

whose symbols have the same meaning as in Eq. (11).

The sum of these two decompositions is equal to the total error from Eq. (10) to within the output numerical precision of RAZOR, as shown in Eq. (13):

$$E_{\text{total}} = E_{\text{model}} + E_{\text{interaction}} = \frac{C_{\text{HDMR}} - C_{\text{POD}}}{C_{\text{POD}}}. \tag{13}$$

This decomposed error is computed for both C_L and C_D for each of the 19 points from the Latin hypercube sampling (Fig. 9) whose total error is greater than 10%, all of which occur for the Lift coefficient, and one of which also occurs for the Drag coefficient, and are shown in Fig. 10. The results clearly show that the majority of the error for these points is due to missing high-order interactions, rather than inaccurate surrogates for low-order sub-domains. Therefore, since in the context of the analysis provided in this paper the effects of changing only one or two parameters at a time are shown, a high degree of reliability of the results with respect to the POD ROM is achieved.

Given this and the fact that the high error points represent approximately 1.9% of the space, as well as 86.1% of the Latin hypercube points giving a relative error smaller than 5%, and the error relative to the four high fidelity CFD Latin hypercube samples shown in the previous section being within 7%, the HDMR surrogate approach is appropriate for the sensitivity analysis in this paper.

4. Aerodynamic sensitivity: drag

For the Drag coefficient, C_D, the central value from equation (8) is calculated as $f_c = 163$ Drag counts, corresponding to the value of C_D at the 'central' point in the parameter space. As per Eq. (8), an approximation of C_D is achieved for any point in the space by summing the central value with all of the other surrogate models. For example, if all of the geometrical parameters are kept at central values except for the sweep, then the graph in Fig. 11 describes the deviation in C_D away from the central value as the sweep is varied.

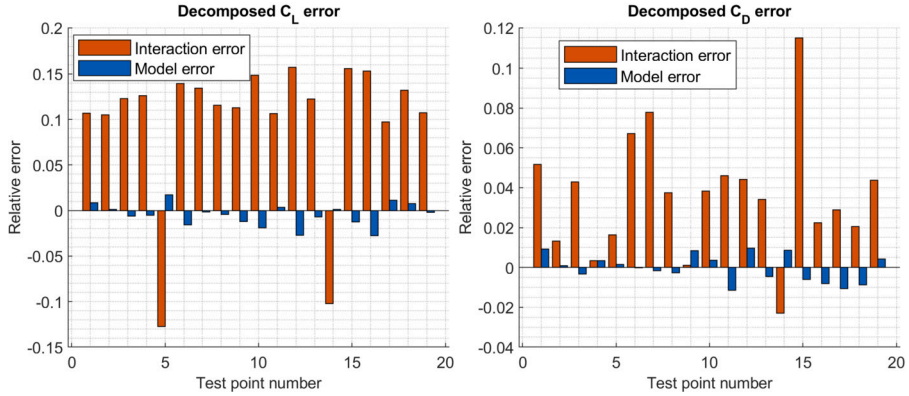

Fig. 10. Plot of the C_L and C_D error decomposition of the 19 latin hypercube points whose total error is greater than 10% for either coefficient.

Table 6
Summary of most important parameters influencing Drag Coefficient resulting from HDMR. Only 1-factor and 2-factor contributions are presented here.

Increment function	Min ΔC_D	Max ΔC_D	Range(ΔC_D)	Range($\sum \Delta C_D$)
Sweep	-16	15	31	31
Tip twist	-6	5	11	11
Root chord	-4	6	10	10
Sweep & Strut angle	-1	5	6	42
Sweep & Root chord	-3	5	8	39
Sweep & Tip twist	-3	3	6	38

Table 7
Summary of the dimensional gradients of the HDMR surrogates at the central point in Drag counts. At the central point, all higher-order incremental contributions to the gradient are zero as a consequence of the HDMR methodology.

Increment function	Gradient
Tip chord (d.c./m)	-29
Tip twist (d.c./°)	13
Root chord (d.c./m)	-12
Kink twist (d.c./°)	5
Sweep (d.c./°)	-3
Span (d.c./m)	2
Strut angle (d.c./°)	2

Table 6 reports the rankings of the 1-factor and 2-factor contributions with respect to their impact on the Drag coefficient, while Table 12 in Appendix A has the complete set of rankings. The sweep has a much larger effect on the Drag than the other individual parameters, with a larger sweep leading to a smaller Drag coefficient. Physically speaking, this is explained by the reduction in wave Drag due to a decreased local Mach number on the wing at larger sweep angles. This is exemplified in Fig. 11, which shows the Drag varies by up to approximately ±15 Drag counts almost linearly.

Table 7 shows the dimensional gradients for C_D of the parameters in the study in Drag counts. Per metre, the tip chord has the largest effect due to the relative influence on the taper ratio. In contrast, the sweep, which has the largest global effect on the Drag, has a relatively small change per degree of sweep.

As shown in Fig. 12, the first-order (non-interacting) sub-domains experience a minimum or maximum at or near their extreme values. The tendency of the Drag to increase with the twist parameters is explained as an increase in the local angle of attack, which in turn leads to an increase in the wing's induced Drag. However, the strut produces much less Lift compared to the wing, so induced Drag alone does not explain why an increase in the strut incidence angle has a similar effect as an increase in the wing twist parameters. With reference to Fig. 13, it is shown that the shock wave at the wing-strut intersection is much

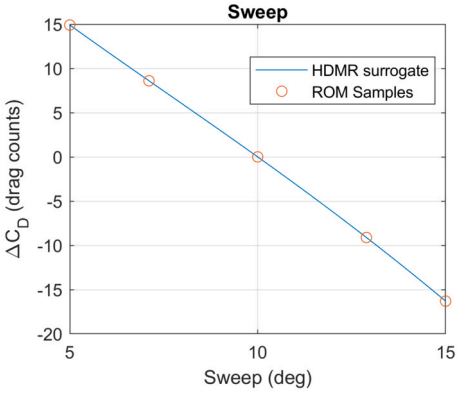

Fig. 11. Plot of the response of C_D with respect to changes in sweep angle.

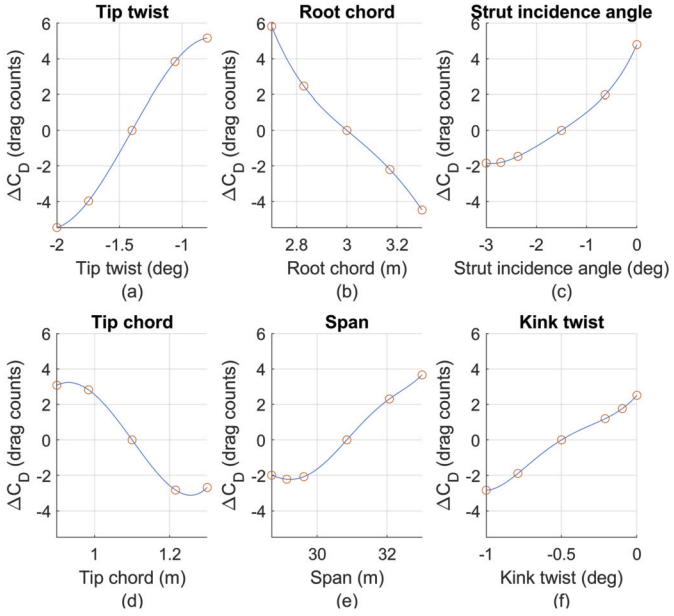

Fig. 12. Plot of the response of C_D with respect to changes in geometrical parameters. The symbols have the same meaning as in Fig. 11.

stronger at the maximum strut incidence angle than at the minimum. The effect of the parameter on C_D is therefore explained by this increase in wave Drag.

Finally, the chord parameters each have the individual effect of reducing the Drag. In Fig. 14 it is observed that although the leading edge chordwise position of the wing-strut intersection relative to the

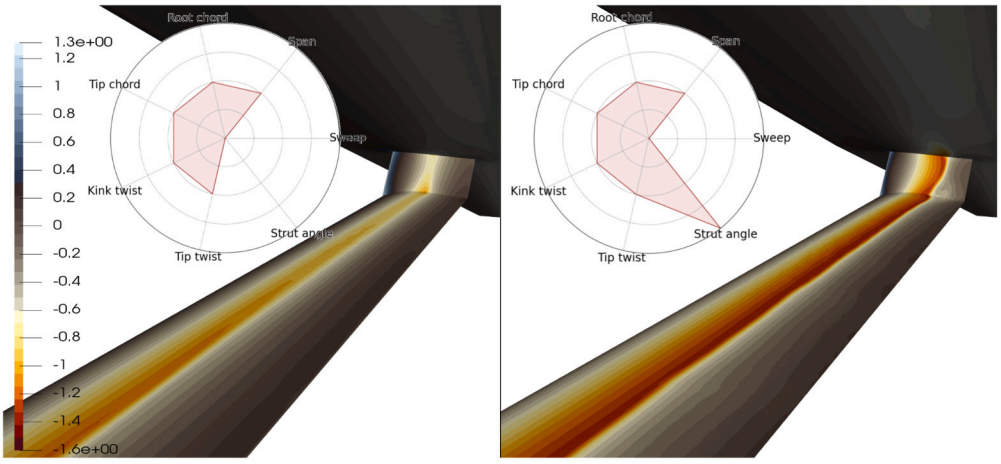

Fig. 13. Plot of high-fidelity CFD solutions for the surface Pressure Coefficient near the strut-wing intersection at the minimum sweep angle. On the left: minimum strut incidence angle, -3°. On the right: maximum strut incidence angle, 0°.

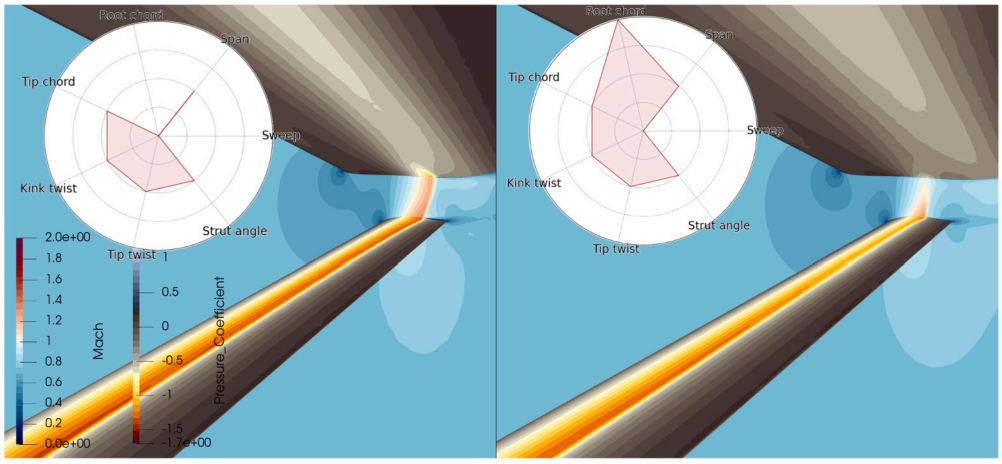

Fig. 14. Plot of high-fidelity CFD solutions at the minimum sweep angle for the surface pressure coefficient near the strut-wing intersection, with a volume slice of the Mach number near the wing-strut intersection. On the left: minimum root chord, 2.7 m. On the right: maximum root chord, 3.3 m.

wing chord remains fixed, the separation of the strut maximum upper camber and wing minimum lower camber increases with the root chord, leading to a reduction in the strength of the shock wave.

Fig. 15 shows the three 2-factor sub-domains with the largest residual effect on C_D. The sweep and root chord interaction seems to indicate that the Drag reduction effect of the root chord is stronger at the minimum sweep angle. High-fidelity CFD solutions at the corners of this space are shown in 16. It is clear that an increase of the root chord has the effect of weakening the shock wave on the strut, with the effect being slightly more pronounced at the minimum sweep where the initial shock is stronger.

Table 8
Summary of most important parameters influencing Lift Coefficient resulting from HDMR. Only 1-factor and 2-factor contributions are presented here.

Increment function	Min ΔC_L	Max ΔC_L	Range(C_L)	Range($\sum C_L$)
Kink twist	-10.2%	7.9%	18.1%	18.1%
Sweep	-5.2%	8.4%	13.6%	13.6%
Tip chord	-2.7%	7.9%	9.4%	9.4%
Kink twist & Root chord	-5.3%	1.8%	7.1%	28.7%
Kink twist & Tip twist	-1.7%	1.4%	3.1%	27.4%
Kink twist & Sweep	-6.7%	4.0%	10.6%	25.7%

5. Aerodynamic sensitivity: lift

For the Lift coefficient, C_L, the central value from equation (8), is calculated as $f_c = 0.344$, corresponding to the value of C_L at the 'central' point in the parameter space. As per Eq. (8), an approximation of C_L is achieved for any point in the space by summing the central value with all of the other surrogate models. For example, if all of the geometrical parameters are kept at central values except for the kink twist, then the graph in Fig. 17 describes the deviation in C_L away from the central value as the kink twist is varied.

Table 8 reports the results of the HDMR analysis for the Lift coefficient, highlighting the highest ranked parameters for the 1-factor and 2-factor contributions. A complete ranking is provided instead in Table 13 in Appendix A. The kink twist has the largest effect on the Lift coefficient, followed by the sweep and then the tip chord, all with a $> 10\%$ influence on C_L. The effect of the kink twist is expected, since changes in local angle of attack tend to have a big influence on the Lift. The tip twist has a smaller effect because of the washout of the outboard portion of the wing.

Table 9 shows the dimensional gradients for C_L of the parameters in the study. Per metre, the tip chord has the largest effect due to the relative influence on the taper ratio, although it is observed in Fig. 18 that the gradient levels off towards the extreme values.

An increased sweep angle serves to reduce the local Mach number over the wing, leading to weaker pressure gradients and therefore a reduced Lift coefficient. The effect of the tip twist and strut incidence angle is again explained by increases in local angle of attack. It is seen from Fig. 19 that an increased root chord causes less of the wing to ex-

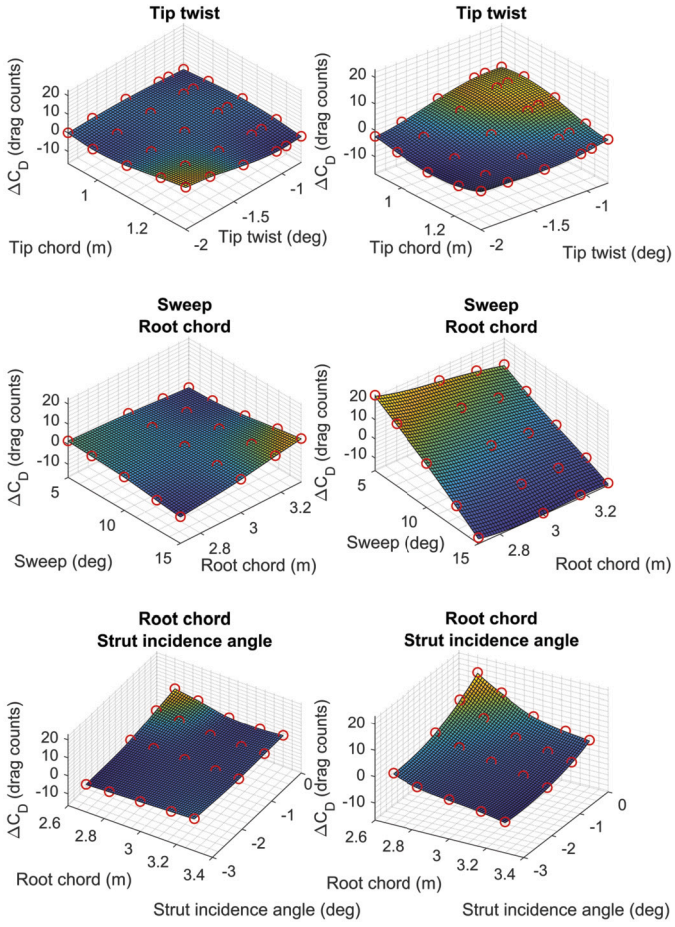

Fig. 15. Plot of the response of C_D with respect to changes in pairs of geometrical parameters. In the left column: excluding individual contributions. In the right column: including individual contributions. The red circle symbols represent POD function samples, whereas the surface represents a grid of HDMR surrogate samples.

Table 9
Summary of the dimensional gradients of the HDMR surrogates at the central point. At the central point, all higher-order incremental contributions to the gradient are zero as a consequence of the HDMR methodology.

Increment function	Gradient
Tip chord (/m)	-32.04%
Kink twist (/°)	16.97%
Root chord (/m)	14.26%
Tip twist (/°)	8.24%
Sweep (/°)	-2.03%
Strut angle (/°)	1.27%
Span (/m)	-1.12%

perience low pressure due to interference, thereby increasing the Lift coefficient. There is also a stronger expansion in the wing-strut intersection at the minimum root chord, contributing to the same effect.

Fig. 20 shows the three two-factor sub-domains with the largest residual effect on C_L. Interestingly, the magnitude of the incremental interacting contributions is comparable to the overall effect including the one-factor increment functions.

6. Sensitivity of lift-to-drag ratio

The sensitivity on the Lift-to-Drag ratio is generated from the ratio of matching HDMR sub-domain surrogates for C_L and C_D including

Table 10
Summary of most important parameters influencing C_L/C_D resulting from the ratio of the HDMR C_L and C_D surrogates. Only 1-factor and 2-factor contributions are presented.

Increment function	Min $\Delta\frac{L}{D}$	Max $\Delta\frac{L}{D}$	Range($\frac{L}{D}$)	Range($\sum\frac{L}{D}$)
Root chord	-5.34%	10.49%	15.83%	15.83%
Kink twist	-8.63%	6.21%	14.84%	14.84%
Span	-1.23%	6.58%	7.81%	7.81%
Root chord & Kink twist	-5.06%	0.26%	5.32%	30.32%
Sweep & Kink twist	-7.88%	3.37%	11.26%	25.13%
Span & Root chord	-4.16%	0.36%	4.52%	22.74%
Span & Kink twist	-2.17%	0.023%	2.20%	22.00%

Table 11
Summary of the dimensional gradients of the HDMR surrogates at the central point.

Increment function	Gradient
Root chord (/m)	21.57%
Tip chord (/m)	-13.89%
Kink twist (/°)	13.77%
Span (/m)	-2.474%
Tip twist (/°)	0.5123%
Sweep (/°)	-0.1635%
Strut angle (/°)	0.1173%

their respective central values, and then the computed central value for C_L/C_D is subtracted from this result. The central value calculated for C_L/C_D is 21.2.

Table 10 shows the most important contributors to the Lift-to-Drag ratio, highlighting the highest ranked 1-factor and 2-factor contributions, whereas the complete ranking is provided in Table 14 in Appendix A.

As observed in previous sections, an increased root chord has the effect of both increasing the Lift and reducing the Drag, leading to the parameter becoming the largest contributor to the Lift-to-Drag ratio. The kink twist causes a much larger increase in Lift than in Drag, so it also becomes a large contributor to the ratio.

Table 11 shows the dimensional gradients for L/D of the parameters in the study. Per metre, the root chord has the largest effect, in contrast to the largest gradient for both C_L and C_D which was the tip chord.

7. Concluding remarks

A global sensitivity analysis of Lift coefficient C_L and Drag coefficient C_D and in turn Lift-to-Drag ratio L/D is performed to understand the effect of seven geometrical parameters on the aerodynamic behaviour and performance characteristics of a high aspect-ratio strut-braced wing. The POD-based reduced-order model is called by the high-dimensional model representation method to generate a series of surrogates for a number of sub-domains of the parameter space, allowing for a detailed investigation of the individual contributions to the coefficients and their interactions in a cost-effective and accurate manner.

The Drag coefficient is influenced primarily by the sweep angle. This is due to the changes in the strength of the shock wave on the wing and the strut caused by changes in the local normal Mach number. Of particular interest is the effect coming from the root chord, which implicitly increases the distance from the strut maximum upper camber and the wing minimum lower camber, reducing the interference-induced shock on the strut caused by compression of the streamlines in the wing-strut window.

On the other hand, the Lift coefficient is primarily influenced by the kink twist, which affects the Lift coefficient by changing the local angle of attack on the wing. Again, the root chord parameter exhibits some interesting behaviour where the interference on the wing pressure side

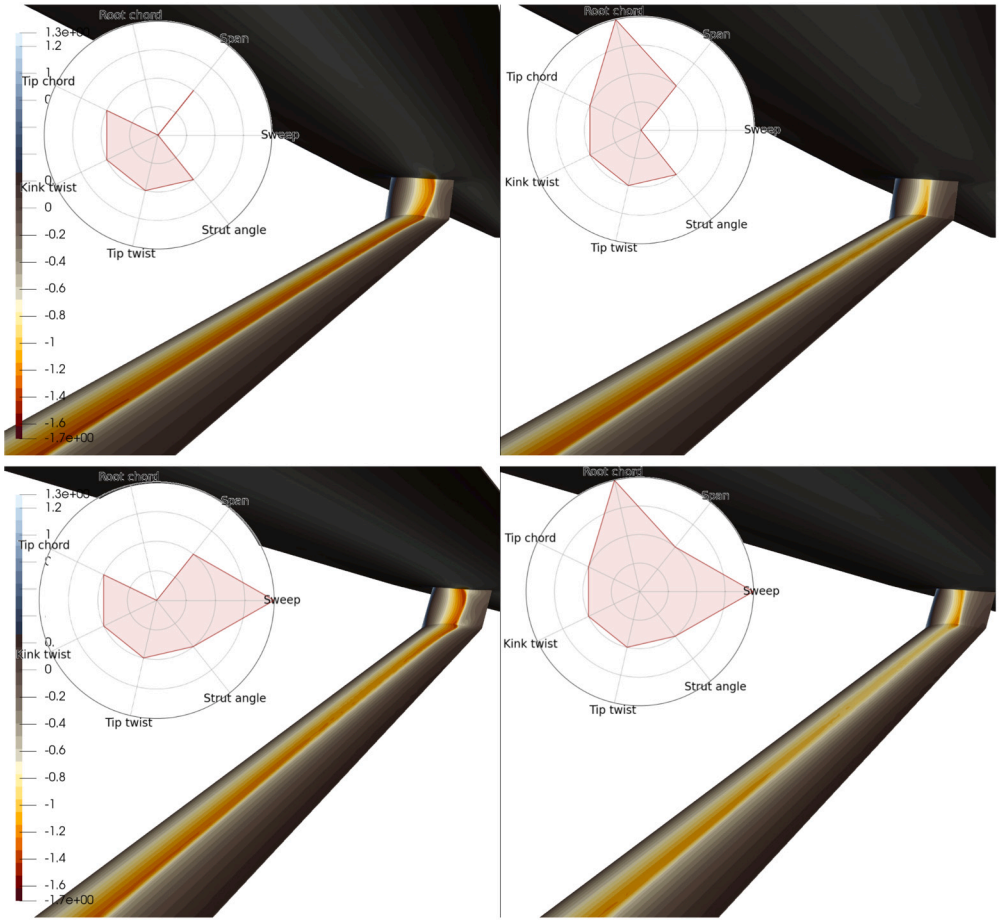

Fig. 16. Plot of high-fidelity CFD solutions for the surface pressure coefficient near the strut-wing intersection. Left column: minimum root chord, 2.7 m. Right column: maximum root chord, 3.3 m. Top row: minimum sweep, 5°. Bottom row: maximum sweep, 15°.

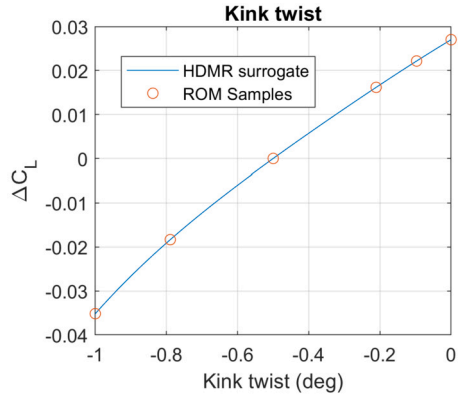

Fig. 17. Plot of the response of C_L with respect to changes in kink twist.

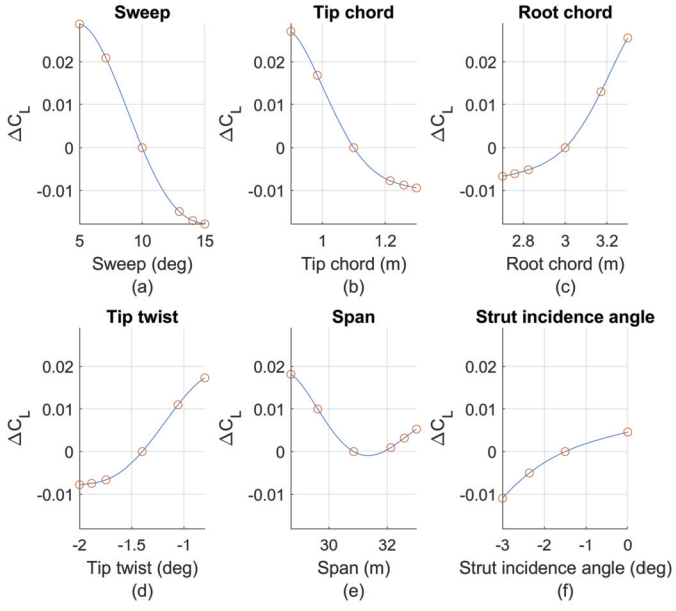

Fig. 18. Plot of the response of C_L with respect to changes in geometrical parameters. The symbols have the same meaning as in Fig. 17.

from the strut is smaller relative to the total wing area as the root chord length increases, thereby increasing the Lift coefficient.

When looking at the Lift-to-Drag ratio, the root chord becomes the dominant factor. As discussed previously, the implicit change in relative wing-strut geometry caused by an increased root chord serves to both reduce the Drag and increase the Lift, causing a compounding effect in their ratio. The kink twist significantly affects the Lift-to-Drag ratio due to having a much larger increase in Lift than in Drag.

It is also observed that the global behaviour within the entire bounds of the parameter space is in some cases significantly different from the local gradients around the central design point. Therefore, it is important to consider the context surrounding this data, especially how the aircraft design and flow physics may lead to a given conclusion.

Overall, the shock wave and aerodynamic interference due to the strut plays a major role in the global strut-braced wing aircraft sen-

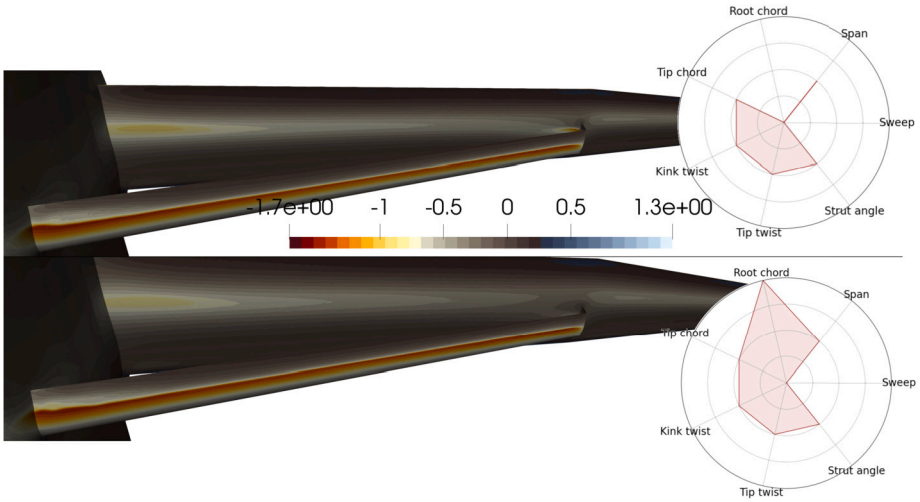

Fig. 19. Plot of high-fidelity CFD solutions for the surface pressure coefficient on the pressure side of the wing at the minimum sweep angle. Top image: minimum root chord, 2.7 m. Bottom image: maximum root chord, 3.3 m.

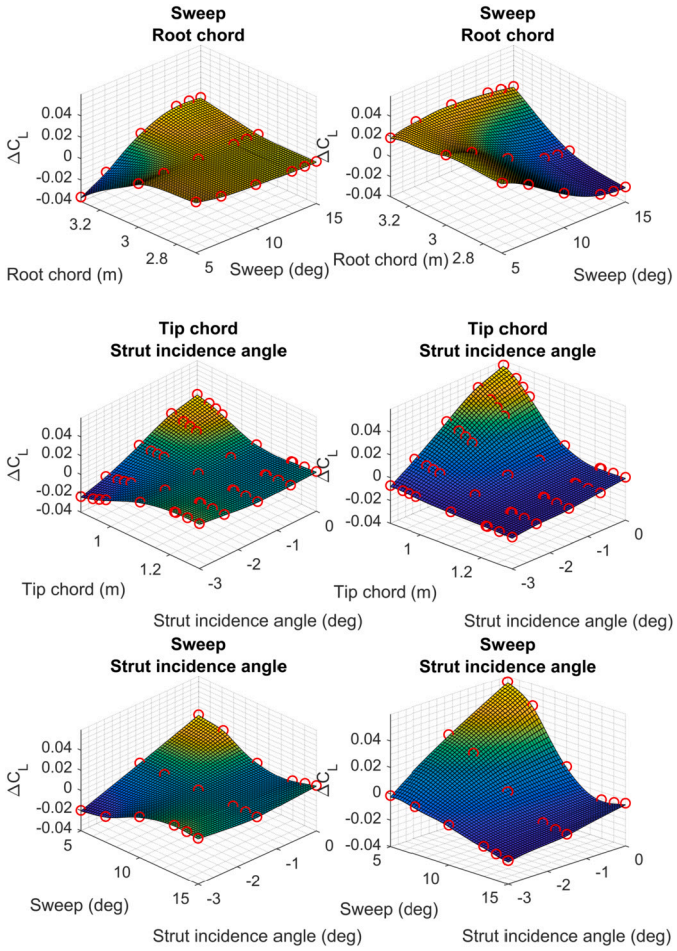

Fig. 20. Plot of the response of C_L with respect to changes in pairs of geometrical parameters. In the left column: excluding individual contributions. In the right column: including individual contributions. The red circle symbols represent POD function samples, whereas the surface represents a grid of HDMR surrogate samples.

sitivity. Implicit changes in the relative geometry between the wing and strut arising from changes in the wing geometrical parameters lead to marked changes in the overall performance of the aircraft. These changes in performance appear to be caused largely by transonic effects arising from interactions between the wing and the strut.

Future work considers a direct comparison of the sensitivity between the strut-braced wing configuration and the same wing with the strut removed. Although removing the strut sacrifices the structural performance prohibitively, the analysis would allow for a comparison of the aerodynamics, isolating more clearly the effect of the strut. This work considered a set of geometrical parameters intended for preliminary design, but a similar study which instead parameterises directly the wing-strut geometry, such as the wing-strut intersection relative chord and span, or the vertical attachment height, could also prove useful. Finally, a higher fidelity global sensitivity analysis which includes for example the aeroelasticity would provide greater insight into ultra-high aspect ratio strut-braced wing configurations.

8. Appendices

8.1. Sensitivity tables

Table 12
Sensitivities for the Drag coefficient (Drag counts), sorted in two tiers by the subdomain order and Range($\sum C_D$). The min/max ΔC_D comes from an optimisation of the given sub-domain surrogate, whose difference also forms Range(C_D). Range($\sum C_D$) is calculated in the same way, except also including each related lower-order surrogate, e.g. for sub-domain (1,2), the surrogates for sub-domain (1,2), (1) and (2) are summed together in the optimisation process.

Increment function	Min ΔC_D	Max ΔC_D	Range(C_D)	Range($\sum C_D$)
1 (Sweep)	-16.3006	14.9086	31.2091	31.2091
6 (Tip twist)	-5.4659	5.1634	10.6293	10.6293
3 (Root chord)	-4.4779	5.8226	10.3005	10.3005
7 (Strut angle)	-1.8618	4.796	6.6578	6.6578
4 (Tip chord)	-3.1222	3.2362	6.3584	6.3584
2 (Span)	-2.2278	3.6626	5.8905	5.8905
5 (Kink twist)	-2.8364	2.5096	5.346	5.346
1 (Sweep) 7 (Strut angle)	-1.2738	5.1039	6.3777	42.0438
1 (Sweep) 3 (Root chord)	-3.3923	4.9739	8.3662	38.6682
1 (Sweep) 6 (Tip twist)	-3.0552	2.6945	5.7496	38.6361
1 (Sweep) 2 (Span)	-1.4149	2.9123	4.3272	38.2668
1 (Sweep) 5 (Kink twist)	-0.58845	2.1422	2.7306	37.4579
1 (Sweep) 4 (Tip chord)	-0.48975	1.5048	1.9946	36.8169
3 (Root chord) 7 (Strut angle)	-1.215	5.3925	6.6076	21.3593

Table 12 (*continued*)

Increment function	Min ΔC_D	Max ΔC_D	Range(C_D)	Range($\sum C_D$)
3 (Root chord) 6 (Tip twist)	-0.57492	1.576	2.1509	18.7751
2 (Span) 3 (Root chord)	-2.8848	2.5197	5.4045	16.8814
6 (Tip twist) 7 (Strut angle)	-1.5424	3.0654	4.6077	16.8284
4 (Tip chord) 7 (Strut angle)	-1.7793	4.3968	6.1761	15.9105
5 (Kink twist) 6 (Tip twist)	-0.78485	3.3499	4.1347	14.7859
2 (Span) 7 (Strut angle)	-1.2127	5.3424	6.5551	14.5564
3 (Root chord) 5 (Kink twist)	-1.57	4.3552	5.9252	14.4589
2 (Span) 6 (Tip twist)	-1.1661	2.7907	3.9568	13.6048
3 (Root chord) 4 (Tip chord)	-2.031	2.3814	4.4124	13.508
4 (Tip chord) 5 (Kink twist)	-1.0419	2.4953	3.5372	13.0575
4 (Tip chord) 6 (Tip twist)	-3.1455	6.1139	9.2594	12.6222
5 (Kink twist) 7 (Strut angle)	-0.001356	2.4041	2.4054	12.618
2 (Span) 5 (Kink twist)	-1.2531	3.3403	4.5934	12.0594
2 (Span) 4 (Tip chord)	-1.9136	2.9372	4.8508	9.3062
1 (Sweep) 2 (Span) 7 (Strut angle)	-3.6831	1.3037	4.9868	48.5736
2 (Span) 4 (Tip chord) 6 (Tip twist)	-2.0825	1.4784	3.5609	14.7115
All surrogates	-25.8982	68.5092	-	94.4075

Table 13
Sensitivities for the Lift coefficient as a % of the central value of 0.344, sorted in two tiers by the subdomain order and Range($\sum C_L$). The min/max ΔC_L comes from an optimisation of the given sub-domain surrogate, whose difference also forms Range(C_L). Range($\sum C_L$) is calculated in the same way, except also including each related lower-order surrogate, e.g. for sub-domain (1,2), the surrogates for sub-domain (1,2), (1) and (2) are summed together in the optimisation process.

Increment function	Min ΔC_L	Max ΔC_L	Range(C_L)	Range($\sum C_L$)
5 (Kink twist)	-10.23%	7.856%	18.08%	18.08%
1 (Sweep)	-5.202%	8.386%	13.59%	13.59%
4 (Tip chord)	-2.74%	7.886%	10.63%	10.63%
3 (Root chord)	-1.943%	7.436%	9.379%	9.379%
6 (Tip twist)	-2.254%	5.026%	7.28%	7.28%
2 (Span)	-0.2723%	5.275%	5.548%	5.548%
7 (Strut angle)	-3.182%	1.334%	4.516%	4.516%
3 (Root chord) 5 (Kink twist)	-5.289%	1.817%	7.106%	28.69%
5 (Kink twist) 6 (Tip twist)	-1.743%	1.403%	3.146%	27.38%
1 (Sweep) 5 (Kink twist)	-6.663%	3.959%	10.62%	25.74%
4 (Tip chord) 5 (Kink twist)	-3.962%	2.107%	6.069%	25.16%
2 (Span) 5 (Kink twist)	-1.904%	0.07655%	1.981%	23.64%
1 (Sweep) 7 (Strut angle)	-5.942%	6.2%	12.14%	22.74%
5 (Kink twist) 7 (Strut angle)	-0.02997%	1.734%	1.764%	21.95%
4 (Tip chord) 7 (Strut angle)	-6.997%	6.839%	13.84%	19.91%
3 (Root chord) 7 (Strut angle)	-5.099%	5.279%	10.38%	19.69%
4 (Tip chord) 6 (Tip twist)	-4.765%	0.2172%	4.982%	18.68%
1 (Sweep) 4 (Tip chord)	-5.023%	4.041%	9.065%	18.45%
3 (Root chord) 4 (Tip chord)	-3.507%	0.5764%	4.083%	17.19%
6 (Tip twist) 7 (Strut angle)	-2.939%	4.339%	7.277%	16.93%
1 (Sweep) 3 (Root chord)	-10.64%	3.484%	14.13%	16.18%
2 (Span) 7 (Strut angle)	-4.993%	5.944%	10.94%	16%

Table 13 (*continued*)

Increment function	Min ΔC_D	Max ΔC_D	Range(C_D)	Range($\sum C_D$)
1 (Sweep) 6 (Tip twist)	-4.038%	3.189%	7.227%	15.49%
1 (Sweep) 2 (Span)	-4.157%	2.211%	6.368%	15.16%
2 (Span) 3 (Root chord)	-3.292%	0.2458%	3.538%	13.48%
3 (Root chord) 6 (Tip twist)	-2.483%	0.8972%	3.38%	13.37%
2 (Span) 4 (Tip chord)	-4.55%	0.6182%	5.168%	11.67%
2 (Span) 6 (Tip twist)	-4.893%	3.023%	7.916%	9.784%
1 (Sweep) 3 (Root chord) 5 (Kink twist)	-4.815%	7.003%	11.82%	36.72%
4 (Tip chord) 5 (Kink twist) 6 (Tip twist)	-0.8299%	1.922%	2.752%	34.77%
3 (Root chord) 5 (Kink twist) 6 (Tip twist)	-1.135%	2.073%	3.208%	33.66%
2 (Span) 3 (Root chord) 5 (Kink twist)	-0.4796%	3.305%	3.785%	32.85%
1 (Sweep) 5 (Kink twist) 6 (Tip twist)	-1.269%	3.238%	4.507%	32.67%
3 (Root chord) 4 (Tip chord) 5 (Kink twist)	-0.3867%	2.328%	2.715%	31.98%
1 (Sweep) 4 (Tip chord) 5 (Kink twist)	-2.716%	3.721%	6.437%	30.1%
1 (Sweep) 2 (Span) 5 (Kink twist)	-1.448%	2.643%	4.09%	29.52%
2 (Span) 5 (Kink twist) 6 (Tip twist)	-1.201%	2.616%	3.817%	29.2%
2 (Span) 4 (Tip chord) 5 (Kink twist)	-0.616%	1.916%	2.532%	28.08%
1 (Sweep) 4 (Tip chord) 6 (Tip twist)	-1.467%	2.349%	3.816%	22.79%
1 (Sweep) 3 (Root chord) 4 (Tip chord)	-2.136%	4.103%	6.239%	21.14%
1 (Sweep) 2 (Span) 3 (Root chord)	-1.065%	2.738%	3.803%	19.14%
2 (Span) 4 (Tip chord) 6 (Tip twist)	-1.24%	3.343%	4.584%	19.03%
1 (Sweep) 2 (Span) 4 (Tip chord)	-1.393%	2.723%	4.115%	18.64%
1 (Sweep) 3 (Root chord) 6 (Tip twist)	-1.721%	3.481%	5.202%	18.59%
2 (Span) 3 (Root chord) 4 (Tip chord)	-0.3959%	2.89%	3.286%	17.58%
2 (Span) 3 (Root chord) 6 (Tip twist)	-1.371%	3.237%	4.608%	16.23%
1 (Sweep) 2 (Span) 6 (Tip twist)	-2.64%	3.558%	6.197%	15.86%
All surrogates	-30.22%	51.93%	-	82.15%

Table 14
Sensitivities for the ratio of the two surrogates C_L/C_D as a % of the central value of 21.2, sorted in two tiers by the subdomain order and Range($\sum L/D$). The min/max $\Delta L/D$ comes from an optimisation of the ratio of given sub-domain surrogate for C_L and C_D, whose difference also forms Range(L/D). Range($\sum L/D$) is calculated in the same way, except also including each related lower-order surrogate, e.g. for sub-domain (1,2), the surrogates for sub-domain (1,2), (1) and (2) are summed together for C_L and divided by the same result for C_D in the optimisation process.

Increment function	Min $\Delta \frac{L}{D}$	Max $\Delta \frac{L}{D}$	Range($\frac{L}{D}$)	Range($\sum \frac{L}{D}$)
3 (Root chord)	-5.34%	10.49%	15.83%	15.83%
5 (Kink twist)	-8.63%	6.21%	14.84%	14.84%
2 (Span)	-1.23%	6.58%	7.81%	7.81%
4 (Tip chord)	-1.10%	5.88%	6.98%	6.98%
1 (Sweep)	-0.74%	5.39%	6.12%	6.12%
7 (Strut angle)	-2.07%	0.0066%	2.08%	2.08%
6 (Tip twist)	-0.010%	1.79%	1.80%	1.80%
3 (Root chord) 5 (Kink twist)	-5.06%	0.26%	5.32%	30.32%
1 (Sweep) 5 (Kink twist)	-7.88%	3.37%	11.26%	25.13%

(*continued on next page*)

Table 14 (*continued*)

Increment function	Min ΔC_D	Max ΔC_D	Range(C_D)	Range($\sum C_D$)
2 (Span) 3 (Root chord)	-4.16%	0.36%	4.52%	22.74%
2 (Span) 5 (Kink twist)	-2.17%	0.023%	2.20%	22.00%
3 (Root chord) 7 (Strut angle)	-5.84%	4.77%	10.61%	21.49%
1 (Sweep) 3 (Root chord)	-9.30%	1.74%	11.03%	21.20%
3 (Root chord) 4 (Tip chord)	-3.49%	0.085%	3.57%	20.24%
5 (Kink twist) 6 (Tip twist)	-3.73%	1.39%	5.13%	18.25%
4 (Tip chord) 5 (Kink twist)	-5.29%	0.57%	5.87%	18.11%
5 (Kink twist) 7 (Strut angle)	-0.97%	1.06%	2.03%	17.44%
1 (Sweep) 2 (Span)	-5.85%	1.76%	7.61%	16.39%
1 (Sweep) 4 (Tip chord)	-5.57%	3.22%	8.79%	16.18%
3 (Root chord) 6 (Tip twist)	-2.31%	0.12%	2.44%	15.86%
1 (Sweep) 7 (Strut angle)	-6.31%	2.96%	9.26%	14.89%
4 (Tip chord) 6 (Tip twist)	-4.72%	1.42%	6.14%	13.24%
1 (Sweep) 6 (Tip twist)	-3.42%	3.11%	6.53%	12.65%
4 (Tip chord) 7 (Strut angle)	-5.97%	4.01%	9.98%	12.34%
2 (Span) 7 (Strut angle)	-4.47%	2.57%	7.04%	12.15%
2 (Span) 4 (Tip chord)	-4.11%	0.41%	4.52%	10.59%
2 (Span) 6 (Tip twist)	-6.50%	2.85%	9.35%	7.83%
6 (Tip twist) 7 (Strut angle)	-2.64%	3.75%	6.38%	7.54%
2 (Span) 4 (Tip chord) 6 (Tip twist)	-0.75%	3.98%	4.72%	15.41%
All surrogates	-56.34%	34.18%	-	90.52%

8.2. Verification design vectors (Table 15)

Table 15
Design vectors for the verification of the surrogate models.

Sample	Sweep (°)	Span (m)	Root chord (m)	Tip chord (m)	Kink twist (°)	Tip twist (°)	Strut angle (°)
1	13.6546	31.4279	3.1656	1.2888	-0.072910	-1.1544	-1.0218
2	13.8973	31.1772	3.0783	1.2250	-0.3943	-0.9819	-0.093077
3	12.2409	32.4461	3.2583	1.1687	-0.2599	-1.2605	-0.4454
4	10.0458	32.6485	3.0259	1.1326	-0.1984	-0.8716	-1.1444

Declaration of competing interest

The authors declare that they have no known competing financial interests or personal relationships that could have appeared to influence the work reported in this paper.

Data availability

Data will be made available on request.

Acknowledgements

The present work is part of a CleanSky2 project RHEA. RHEA has received funding from the Clean Sky 2 Joint Undertaking (JU) under grant agreement No 883670. The JU receives support from the European Union's Horizon 2020 research and innovation programme and the Clean Sky 2 JU members other than the Union.

Numerical simulations made use of Cirrus UK National Tier-2 HPC Service funded by the University of Edinburgh and EPSRC (EP/P020267/1) and ARCHIE-WeSt High Performance Computer based at the University of Strathclyde.

References

[1] FAA, 2021 aviation climate action plan, faa.gov/sites/faa.gov/files/2021-11/Aviation_Climate_Action_Plan.pdf, 2021.
[2] Destination 2050, A route to net zero European aviation, destination2050.eu/wp-content/uploads/2021/02/Destination2050_ExecutiveSummary_Commitments-1.pdf, 2021.
[3] A. Abbas, J. de Vicente, E. Valero, Aerodynamic technologies to improve aircraft performance, Aerosp. Sci. Technol. 28 (1) (2013) 100–132, https://doi.org/10.1016/j.ast.2012.10.008.
[4] J. Xiong, J. Fugate, N. Nguyen, Investigation of Transonic Truss-Braced Wing Aircraft Transonic Wing-Strut Interference Effects Using Fun3d, AIAA Aviation Forum, 2019.
[5] M. Méheut, G. Arnoult, O. Atinault, Q. Bennehard, C. François, Overview of aerodynamic design activities performed at onera to reduce aviation's climate impact, ICAS (2022), icas.org/ICAS_ARCHIVE/ICAS2022/data/papers/ICAS2022_0843_paper.pdf.
[6] G. Carrier, G. Arnoult, N. Fabbiane, J.-S. Schotté, C. David, S. Defoort, M. Delavenne, E. Bénard, Multidisciplinary Analysis and Design of Strut-Braced Wing Concept for Medium Range Aircraft, AIAA Scitech, 2022.
[7] M.K. Bradley, C.K. Droney, T.J. Allen, Subsonic ultra green aircraft research: phase II – volume I – truss braced wing design exploration, ntrs.nasa.gov/citations/20150017036, 2015.
[8] B. Iooss, P. Lemaître, A Review on Global Sensitivity Analysis Methods, Springer US, Boston, MA, 2015, pp. 101–122.
[9] C. Gong, B.-F. Ma, Shape optimization and sensitivity analysis of a morphing-wing aircraft, Int. J. Aeronaut. Space Sci. 20 (2019) 57–69, https://doi.org/10.1007/s42405-018-0110-7.
[10] I. Chakraborty, T. Nam, J.R. Gross, D.N. Mavris, J.A. Schetz, R.K. Kapania, Comparative assessment of strut-braced and truss-braced wing configurations using multidisciplinary design optimization, J. Aircr. 52 (6) (2015) 2009–2020, https://doi.org/10.2514/1.C033120.
[11] S. Hosseini, M.A. Vaziri-Zanjani, H.R. Ovesy, Conceptual design and analysis of an affordable truss-braced wing regional jet aircraft, Proc. Inst. Mech. Eng., G J. Aerosp. Eng. (2020) 1–20, https://doi.org/10.1177/0954410020923060.
[12] T. Chau, D.W. Zingg, Aerodynamic design optimization of a transonic strut-braced-wing regional aircraft, J. Aircr. 59 (1) (2022) 253–271, https://doi.org/10.2514/1.C036389.
[13] N.R. Secco, J.R.R.A. Martins, Rans-based aerodynamic shape optimization of a strut-braced wing with overset meshes, J. Aircr. 56 (1) (2019) 217–227, https://doi.org/10.2514/1.C034934.
[14] M. Kubicek, High Dimensional Uncertainty Propagation for Hypersonic Flows and Entry Propagation, University of Strathclyde, 2018, https://doi.org/10.48730/9dy2-st94.
[15] M. Kubicek, E. Minisci, M. Cisternino, High dimensional sensitivity analysis using surrogate modeling and high dimensional model representation, Int. J. Uncertainty Quanitification 5 (5) (2015) 393–414, https://doi.org/10.1615/Int.J.UncertaintyQuantification.2015012033.
[16] M. Fossati, Evaluation of aerodynamic loads via reduced-order methodology, AIAA J. 53 (2015) 1–17, https://doi.org/10.2514/1.J053755.
[17] Y. Ma, S. Karpuk, A. Elham, Conceptual design and comparative study of strut-braced wing and twin-fuselage aircraft configurations with ultra-high aspect ratio wings, Aerosp. Sci. Technol. 121 (2022), https://doi.org/10.1016/j.ast.2022.107395.
[18] T. Bui-Thanh, M. Damodarany, Proper orthogonal decomposition extensions for parametric applications in transonic aerodynamics 2003, https://doi.org/10.2514/6.2003-4213, 06 2003.
[19] T.W. Lukaczyk, A.D. Wendorff, M. Colonno, T.D. Economon, J.J. Alonso, T.H. Orra, C. Ilario, Suave: an open-source environment for multi-fidelity conceptual vehicle design, in: 16th AIAA/ISSMO Multidisciplinary Analysis and Optimization Conference, 2015.
[20] P. Holmes, J.L. Lumley, G. Berkooz, Turbulence, Coherent Structures, Dynamical Systems and Symmetry, Cambridge Monographs on Mechanics, Cambridge University Press, 1996.
[21] T.D. Economon, F. Palacios, S.R. Copeland, T.W. Lukaczyk, J.J. Alonso, Su2: an open-source suite for multiphysics simulation and design, AIAA J. 54 (3) (2016), https://doi.org/10.2514/1.J053813.
[22] L. Sirovich, Turbulence and the dynamics of coherent structures. I - coherent structures. ii - symmetries and transformations. iii - dynamics and scaling, Q. Appl. Math. 45 (1987), https://doi.org/10.1090/qam/910463.
[23] P.M. Mehta, M. Kubicek, E. Minisci, M. Vasile, Sensitivity analysis and probabilistic re-entry modeling for debris using high dimensional model representation based uncertainty treatment, Adv. Space Res. 59 (1) (2017) 193–211, https://doi.org/10.1016/j.asr.2016.08.032.